Simulations of self-magnetization in expanding high-energy-density plasmas

K. V. Lezhnin,[1, a)] S. R. Totorica,[2, 3] J. Griff-McMahon,[2] M. V. Medvedev,[4, 5] H. Landsberger,[2] A. Diallo,[1] and W. Fox[1, 2, 6]

[1)]*Princeton Plasma Physics Laboratory, 100 Stellarator Rd, Princeton, NJ 08540,*
USA
[2)]*Department of Astrophysical Sciences, Princeton University, Princeton, NJ 08544,*
USA
[3)]*Department of Astro-fusion Plasma Physics (AFP), Headquarters for Co-Creation Strategy,*
National Institutes of Natural Sciences, Tokyo 105-0001, Japan
[4)]*Department of Physics and Astronomy, University of Kansas, Lawrence, KS 66045*
[5)]*Laboratory for Nuclear Science, Massachusetts Institute of Technology, Cambridge,*
MA 02139
[6)]*Department of Physics, University of Maryland, 8279 Paint Branch Drive, College Park, MD 20742,*
USA

(Dated: 21 March 2025)

Understanding plasma self-magnetization is one of the fundamental challenges in both laboratory and astrophysical plasmas. Self-magnetization can modify the plasma transport properties, altering the dynamical evolution of plasmas. Most high energy density (HED) laser experiments on magnetic reconnection and unmagnetized collisionless shocks rely on either Biermann or Weibel mechanisms to self-consistently generate the magnetic fields of interest. Multiple HED experiments have observed the formation of ion-scale magnetic filaments of megagauss strength, though their origin remains debated. Models based on Particle-in-Cell (PIC) simulations have been proposed to explain magnetization, including plasma interpenetration-driven Weibel, temperature gradient-driven Weibel, and adiabatic expansion-driven Weibel. Here, we conducted 2D collisional PIC simulations with a laser ray-tracing module to simulate plasma ablation, expansion, and subsequent magnetization. The simulations use a planar geometry, effectively suppressing the Biermann magnetic fields, to focus on anisotropy-driven instabilities. The laser intensity is varied between 10^{13}–10^{14} W/cm^2, which is relevant to HED and ICF experiments where collisions must be considered. We find that above a critical intensity, the plasma rapidly self-magnetizes via an expansion-driven Weibel process, generating plasma beta of 100 ($\beta = 2k_B n_e T_e / B^2$) with the Hall parameter $\omega_{ce}\tau_e > 1$ within the first few hundreds of picoseconds. Implications of plasma magnetization for heat transport are also discussed.

Understanding plasma magnetization is one of the fundamental challenges in both high energy density (HED)[1,2] and astrophysical plasmas[3]. Magnetic fields are found in a wide variety of astrophysical systems, ranging from extremely strong fields ($\sim 10^{11}$ T) in compact astrophysical objects[4] to $\sim 10^{-9}$ T fields that permeate galactic and extragalactic regions[5], with the turbulent dynamo[6], Biermann battery[7], and Weibel instability[8] serving as the primary theoretical hypotheses of plasma magnetization. The magnetization mechanisms are similar in high energy density (HED) plasmas produced in the laboratory. Indeed, Biermann battery field generation is responsible for the plasma magnetization around the laser spot, producing azimuthal fields observed in laboratory astrophysics experiments on magnetic reconnection[9–12] and predicted in the inertial confinement fusion (ICF) hohlraum simulations[13]. Weibel fields are commonly diagnosed in laser experiments involving counterstreaming plasmas[14,15], and can modify strongly driven magnetic reconnection[16] and drive collisionless shock formation in laboratory and astrophysical plasmas[17–19]. A series of recent short pulse experiments tested the theory of thermal Weibel instability[20]. Fi-

nally, seeding turbulence in the plasma has allowed experiments on magnetic field amplification by turbulent dynamo processes[21].

Despite a large body of experimental measurements and numerical models of plasma magnetization, the self-consistent magnetization of expanding plasma in HED laser experiments is still not fully understood. Multiple mechanisms have been proposed to produce temperature anisotropy leading to Weibel instability in plasmas. A general criterion is that given sufficiently rapid plasma evolution, either rapid heat flows, rapid compression, or rarefaction can produce anisotropic distributions if these processes dominate over collisional relaxation. Refs.[22,23] addressed the interplay of the Weibel and Biermann battery mechanisms in collisionless plasma, concluding that the Weibel instability dominates in setups with shallow temperature gradients $L_T/d_i > 1$ ($L_T = T_e/|dT_e/dx|$ is the electron temperature gradient scale and d_i is the ion inertial length[24]). Ref.[25] addressed the role of collisions, and found that growth of the Weibel instability also has a dependence on the Knudsen number, requiring $\lambda_{e,\mathrm{mfp}}/L_T \gtrsim 1$ (here, $\lambda_{e,\mathrm{mfp}}$ is the electron mean free path). These works used kinetic simulations that were initialized from analytic, bell-shaped temperature and density profiles, leading to temperature gradient-driven Weibel instability development in the subsequent evolu-
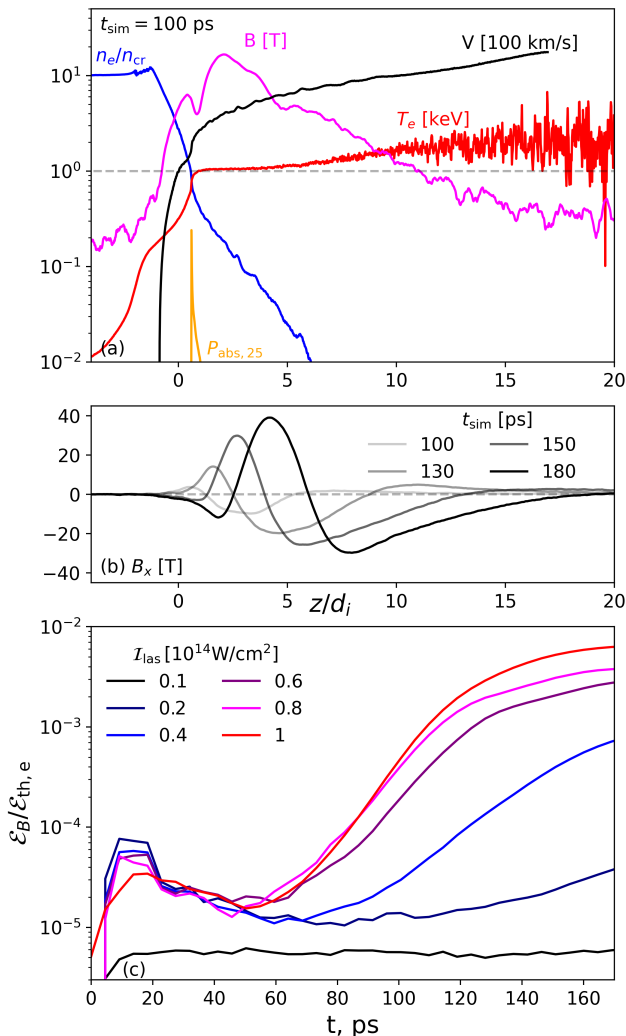
[a)]Electronic mail: klezhnin@pppl.gov

FIG. 1. (a) Plasma profiles from laser ablation in 1D. A laser pulse of 10^{14}W/cm² from the right of the simulation box heats the target, causing underdense plasma to expand outwards (in the $+z$ direction). Magnetic fields appear from the noise level in the underdense part of the target close to the critical surface ($z/d_i \sim 0$). (b) Time evolution of B_x profile. (c) Evolution of magnetic to thermal energy ratio in the $0 \leq z/d_i \leq 35$ region for $I = 10^{13}$W/cm² (case considered in detail in Ref.[31]) and $I = 10^{14}$W/cm² (primary case considered in this paper), along with intermediate values. Magnetic energy reaches nearly 1% of electron internal energy at $t \approx 180$ps for the $I = 10^{14}$W/cm² case, while for $I = 10^{13}$W/cm², it remains at the level of the initial numerical noise.

tion. Recently, Ref.[26] presented observations of ion-scale filaments and argued they arose due to a temperature-gradient-driven electron Weibel instability for plasmas with $\lambda_{e,\mathrm{mfp}}/L_T \gtrsim 0.05$ on the basis of particle simulations initialized from radiation hydrodynamic simulation profiles. Refs.[27,28] considered the case of plasma rapidly expanding into vacuum, showing that the preferential

cooling along the expansion direction could produce temperature anisotropy and Weibel instability. While all these works predict a similar level of expanding plasma magnetization ($\beta_e^{-1} \sim 0.01$, where $\beta_e = 2k_B n_e T_e/B^2$ is the electron plasma beta), the anisotropy development mechanisms, and, as a consequence, magnetic field polarizations, differ. Refs.[22,23,25,26] also focus on fields forming around the focal spot and do not consider the self-consistent laser ablation, which can be modified by the emergence of the magnetic field at or around the ablation front.

Recently, in Refs.[29–31], we developed and validated a laser ray tracing capability for PIC simulations within the code PSC[32]. The laser heating module was benchmarked against hydrodynamic codes FLASH[33,34] and RALEF[35], finding overall good agreement in the expanding plasma profiles in a strongly-collisional regime. In this work, we consider a first-principles kinetic ablation using a collisional particle-in-cell simulation with laser-ray tracing and show that the expanding plasma ubiquitously self-magnetizes above a critical laser intensity. The results build upon the results of Ref.[31], where a 1D laser ablation problem was considered for $I = 10^{13}$ W/cm², showing good agreement with the radiation hydrodynamic code FLASH. In the present work, we expand our investigations to two dimensions and higher laser intensities, showing how an intensity of around 10^{14} W/cm² changes the plasma expansion physics due to plasma self-magnetization. In order to focus on the Weibel-driven self-magnetization, the present 2D simulations use a uniform transverse laser intensity to prevent development of Biermann fields. We show the relevant anisotropy is driven by preferential adiabatic expansion normal to the target surface, which is strong enough to overcome particle collisionality, sustaining sufficient anisotropy levels to drive the Weibel instability. We find that the numerical results are in agreement with predictions of the growth rates from the electron Weibel linear instability theory incorporating collisional effects.

We begin by discussing the problem of laser-driven plasma self-magnetization in one dimension. Figure 1 shows the result of a 1D PSC simulation, demonstrating magnetization of the laser-driven ablated plasma in the high-energy-density regime. The simulation setup is based on Ref.[31], and is described as follows. We consider a 1D $40d_i$-long simulation box. Hereafter, $d_i = c/\sqrt{4\pi n_{\mathrm{cr}}e^2/m_p}$ is the proton inertial length evaluated at the critical density. A solid target of fully ionized Al with an electron density of $10n_{\mathrm{cr}}$ is located between $-4d_i$ and 0. Here, $n_{\mathrm{cr}} = m_e\omega_0^2/4\pi e^2 \approx 1.1 \cdot 10^{21} (\lambda[\mu\mathrm{m}])^{-2}$ cm^{-3} is the critical density for the laser wavelength λ. The laser is launched from the right side of the box, with laser intensity $I = 10^{14}$ W/cm² and laser wavelength $\lambda = 1.064 \,\mu\mathrm{m}$. The numerical grid is 2000 cells long, with 10^5 particles per cell per species at a density of $n_e = n_{\mathrm{cr}}$. Common to PIC simulations, we use a reduced electron-ion mass ratio and speed of light, see Ref.[36] for details. A reduced proton to electron mass ratio $m_p/m_{e*} = 100$
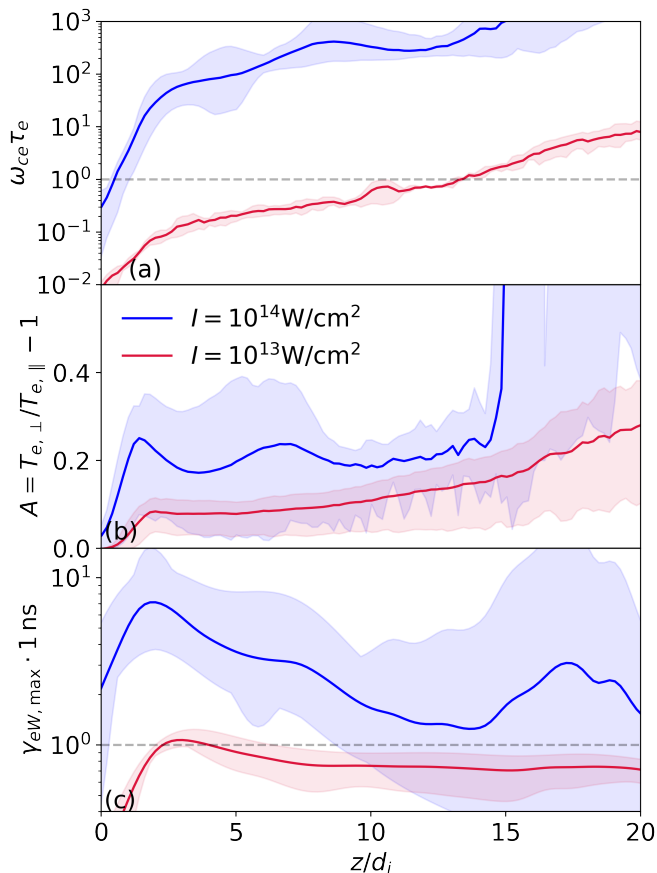
FIG. 2. Transition from unmagnetized to magnetized plasma with laser intensity increase from 10^{13} to 10^{14} W/cm^2. (a) Hall parameter, (b) electron temperature anisotropy, (c) collisionless electron Weibel growth rate for $I = 10^{13}$ (red lines and shaded regions) and 10^{14} W/cm^2 (blue lines & shaded regions) simulations. The 10^{13} W/cm^2 case is shown at 200 ps, and the 10^{14} W/cm^2 case at 100 ps to account for different evolutionary timescales. The shaded regions denote the error bar given by the range of different numerical parameters (mass ratio, speed of light, dimensionality, particle resolution).

is used in the main set of simulations, as well as the reduced electron rest mass $m_{e*}c_*^2 = 60$ keV. See Appendix A for additional information on the convergence studies. The simulation is conducted for $t_{\rm sim} = 200$ ps. Figure 1a presents plasma density, temperature, and expansion speed profiles, as well as laser heating (normalized to 10^{25} erg/s/cm^3) and magnetic field profiles for $t = 100$ ps. A magnetic field structure emerges near the critical surface (location where $n_e(z) = n_{\rm cr}$), reaching 20 T and expanding towards the vacuum where the temperature gradient is largest. At this magnetic field strength, the electron gyrofrequency, $\omega_{\rm ce}$, is large enough, such that $\omega_{\rm ce}t_{\rm sim} > 10$, indicating that the necessary condition for electron magnetization, $\omega_{\rm ce}t_{\rm sim} > 1$, is satisfied. It should be noted that here we provide a conservative estimate of $\omega_{\rm ce}t_{\rm sim}$ from our simulation with "heavy" electrons due to reduced mass ratio, and one may ex-

pect $\omega_{\rm ce}t_{\rm sim} \gtrsim 10^2$ under realistic conditions. Figure 1b reveals the time evolution of the magnetic field structure. For the B_x component, a decaying sine wave-like structure appears and grows around $z = 2\text{-}10\ d_i$. Such a magnetic field structure is observed in B_y as well (B_z is suppressed in pure 1D simulations), and is qualitatively similar to B_x and B_y structure in 2D simulations, as we will show later. These oscillatory structures in magnetic fields are commonly associated with Weibel-like instabilities. Figure 1c tracks the time evolution of magnetic energy normalized to the plasma thermal energy in 1D simulations with various laser intensities. Here, we scanned over several values of the laser intensity, showing the development of self-magnetization with average magnetic energy fraction close to the $\sim 1\%$ level for laser intensities $I \gtrsim 4 \cdot 10^{13}$ W/cm^2.

Figure 2 shows how plasma self-magnetization compares between low and high laser intensities. It depicts profiles of (a) the Hall parameter, $\omega_{\rm ce}\tau_e$ (τ_e is the electron collisional timescale); (b) electron temperature anisotropy ($A \equiv T_{e,\perp}/T_{e,\parallel} - 1$, with the parallel direction being along the expansion/laser/z axis); and (c) normalized collisionless Weibel growth rate for two laser intensities: $I = 10^{13}$ (red) and 10^{14} W/cm^2 (blue). The shaded regions summarize the results of a convergence study varying the reduced numerical parameters (reduced mass ratio, reduced speed of light, particles per cell, dimensionality). The collisionless electron Weibel growth rate calculated for the fastest growing mode, γ_{eW0} (see, e.g., Ref.[25], Eq. 2), is given by:

$$\gamma_{eW0} = \frac{2}{3\sqrt{3\pi}} \frac{v_{th,e}}{c} \omega_{\rm pe} \frac{A^{3/2}}{A+1}, \qquad (1)$$

Here, $v_{th,e} = \sqrt{k_B T_e/m_e}$ is the electron thermal speed, $\omega_{pe} = \sqrt{4\pi e^2 n_e/m_e}$ is the electron plasma frequency, and c is the speed of light in vacuum. In Fig. 2a, the Hall parameter clearly transitions from below 1 to above 10 for an increased laser intensity, indicating a transition to plasma magnetization. The plasma magnetization is robust to varying the numerical parameters as demonstrated by the narrow shaded regions from the convergence study runs. In Fig. 2b, electron temperature anisotropy is present in both laser intensity cases, with higher levels of anisotropy in the $I = 10^{14}$ W/cm^2 case. We note that the anisotropy tends to decrease as the numerical parameters become more realistic (see Figure 6 in Appendix B). Nevertheless, we find that all our simulations develop finite anisotropy with $A > 0$, implying that the expansion direction is "cold" (i.e., $T_{e,\perp} > T_{e,\parallel}$). As is well-known from Weibel instability theory (see, e.g., Ref.[37]), the fastest growing modes align with the "cold" direction, which in our case corresponds to modes with dominant k_z and with transverse magnetic field polarization dominated by B_x and B_y. In 1D simulations, only the k_z mode is allowed, and in 2D simulations, we expect k_z to dominate over k_x. This picture is exactly consistent with our simulations, as we see the development of
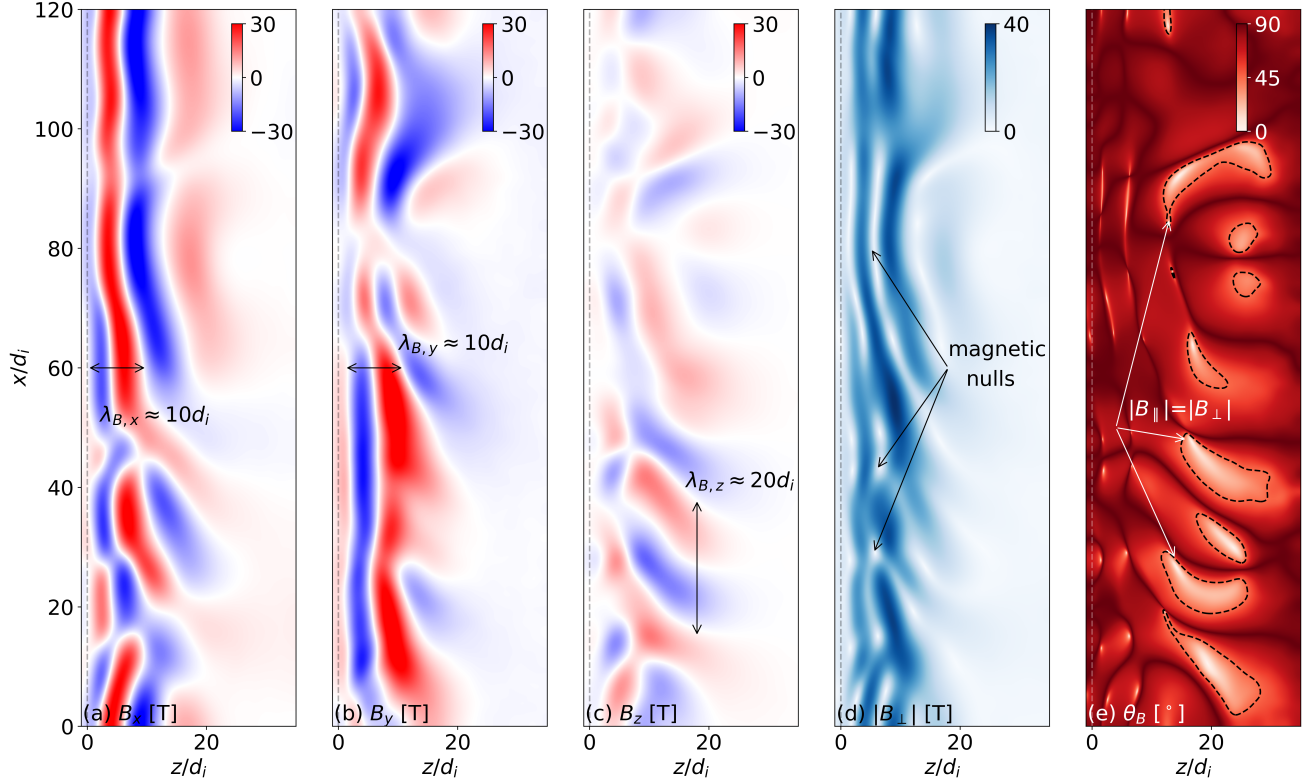
FIG. 3. Magnetic field structure in expanding plasma at t≈ 200 ps - (a)B_x, (b)B_y, (c)B_z, (d) $|B_\perp|$, (e) angle between the magnetic field direction and z axis calculated as θ_B=arctan($|B_\perp|/|B_\parallel|$). Dashed contours in (e) denote regions where $|B_\perp| = |B_\parallel|$.

the k_z mode in 1D (see Fig. 1b) and observe its dominance over the k_x mode in 2D, as we will show later. In Fig. 2c, we see a distinct difference in the collisionless Weibel growth rates between the low and high intensity cases, with $\gamma_{eW0} \sim 10\,\mathrm{ns}^{-1}$ in the high intensity case and $\gamma_{eW0} \sim 1\,\mathrm{ns}^{-1}$ for the lower intensity. To summarize, all the features of Figure 2 are consistent with an electron Weibel instability driving magnetic field generation in our simulations.

Thus far we showed that the expanding plasma in our 1D simulations self-magnetizes, developing a fractional magnetic energy density $\beta_e^{-1} \sim 10^{-2}$, driven by the electron temperature anisotropy $A \geq 0.05$. The Hall parameter and electron Weibel growth rate transition to the plasma magnetization regime when crossing a threshold at $I \approx 4 \cdot 10^{13}\,\mathrm{W/cm}^2$. Now, we investigate the spatial structure and polarization of the magnetic fields to understand its origin as well as possible magnetic trapping effects. Figure 3 reveals the structure of magnetic fields in one of our 2D simulations. These simulations are set up similarly to the 1D version described earlier but add in a transverse dimension along x which has uniform laser intensity. The 2D simula-

tions use a transverse box size of 120 d_i, resolved by 6000 grid nodes, and periodic transverse boundary conditions. 2D simulations open the possibility for all three components of the magnetic field to develop, which are shown in Figs. 3a-c. The magnetic fields reach 40 T in magnitude at the end of the simulation ($t_{\mathrm{sim}} = 200\,\mathrm{ps}$), with the strongest components directed along the x and y axes. The typical wavelength of magnetic fluctuations along z in our simulations revealed by the Fourier analysis is $\lambda_{B,x} \approx \lambda_{B,y} \approx 10d_i$, giving $k_{z,\mathrm{sim}}d_i \approx 0.6$. This value is consistent with the fastest growing mode of Weibel instability[27], $k_{z,\mathrm{fast}}d_i = \sqrt{A}\sqrt{n_e/n_{\mathrm{cr}}}\sqrt{m_i/m_e}$, which may be estimated for our simulation conditions as $k_{z,\mathrm{fast}}d_i \sim 0.5$. 2D simulations also yield inverse plasma beta of $\beta_e^{-1} \sim 10^{-2}$ and anisotropy levels approaching 0.1, in agreement with the 1D runs. The positive sign of the anisotropy parameter A implies $T_\perp > T_\parallel$; thereby, the "cold" direction is along the expansion axis z. In the temperature gradient-driven Weibel instability, thermal transport along ∇T_e (parallel to z) drives perturbations in $f_e(v_z)$. This effectively increases the spread in the particle velocity distribution along z, resulting in an increased parallel temperature, $T_{e,\parallel}$ and a negative value
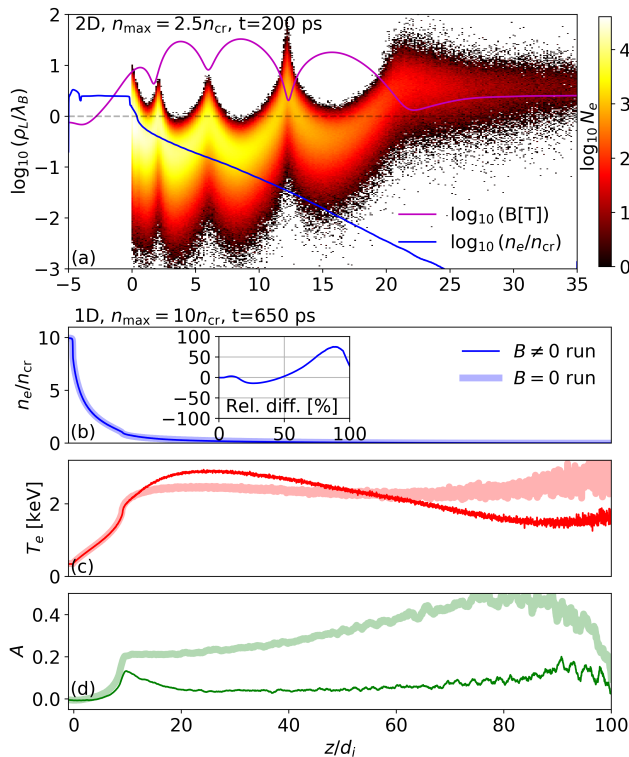
FIG. 4. Magnetic field effects on the electron heat transport. (a) Electron trapping diagram - electron distribution in gyroradius space as a function of distance off the target at $t = 200$ ps. Here, a 2D simulation with $L_x = 40d_i$ and initial target density of $2.5n_{cr}$ is analyzed. Transversely averaged electron density profile (navy) and magnetic field magnitude (magenta) are also shown. (b) Electron density, (c) electron temperature, and (d) anisotropy profiles at $t = 650$ ps comparing 1D simulations with "$B = 0$" (wide transparent lines) against standard 1D simulations (solid lines). The inset of (b) compares relative difference in density profiles. A significant fraction of particles in the underdense plasma is below the $\rho_L = \lambda_B$ threshold for electron trapping via plasma magnetization. A corresponding run at $I = 10^{13}$W/cm^2 (not shown) results in the electron distribution being predominantly unmagnetized on the λ_B scale. Turning off the magnetic fields increases the level of plasma anisotropy and smooths out the electron temperature peak close to the target, while the overall evolution stays similar.

of the anisotropy parameter[22,38]. In the expansion-driven Weibel case[27], expanding plasma adiabatically cools off along the expansion direction, thus decreasing the temperature along z. In our simulations, we observe $A > 0$ across the whole simulation box which suggests that the expansion-driven Weibel process dominates.

Compared to 1D simulations, the 2D simulations open up the possibility to generate parallel magnetic field components, either through transverse modes ($k \perp z$) or through flow shear stretching and folding the primary k_z modes. Figure 3c shows the B_z component of the mag-

netic field, revealing non-negligible field along the expansion direction. In turn, perpendicular magnetic fields of sufficient strength (depicted in Figs. 3a,b,d) can trap electrons, preventing their expansion off the target, thereby modifying the plasma heat transport. The magnetic field inclination relative to the expansion direction is quantified by $\theta_B = \arctan(|B_\perp|/|B_\parallel|)$. With an average value of $72°$, the field is effectively quasi-perpendicular (see Fig. 3e). We therefore expect the magnetic fields to affect electron transport in the ablation front ($0 \leq z/d_i \leq 20$). However, since the perpendicular magnetic field amplitude, $\sqrt{B_x^2 + B_y^2}$, has nulls, as evident from Fig. 3d, electron trapping is not guaranteed throughout the box, even for particles with $\rho_L/\lambda_B < 1$. Here, $\rho_L = m_e v_{e,\perp}/eB$ is the electron Larmor radius. Regions where particle detrapping may occur are highlighted in Fig. 3e by dashed lines, depicting regions with $|B_\parallel| = |B_\perp|$. Nevertheless, as we show next, the overall heat transport appears to be modified by plasma magnetization.

Figure 4 shows how the self-generated magnetic field modifies the plasma dynamics. Fig. 4a depicts the electron distribution along the expansion axis and in the electron gyroradius phase space, calculated for a 2D simulation with $L_x = 40d_i$ and initial electron number density of $2.5n_{cr}$ in the target. A large population of particles (at least 90%) falls below the $\rho_L = \lambda_B$ line, implying that most electrons are magnetized and revolve around magnetic filaments of typical size $\lambda_B = 10d_i$. In contrast, an analogous simulation with $I = 10^{13}$ W/cm^2 (not shown) results in the electron population being predominantly unmagnetized on the scale of the filaments.

It is instructive to understand the repercussions of plasma magnetization on the long-term evolution of ablated plasmas. To quantify the effect of the magnetic field, we ran a 1D simulation up to 650 ps and another simulation with the magnetic contribution inside the particle pusher turned off, see Figs. 4b-d. We find that in the full simulation, the temperature profile develops a spatial gradient in the target normal direction, whereas the "$B = 0$" simulation is highly isothermal (Fig. 4c). The magnetized simulation temperature rises about 20% above the unmagnetized case in a heated region near the critical surface ($z \approx 20d_i$), and falls to $\sim 20\%$ below the unmagnetized case further in the corona ($z = 80d_i$). Such a peak may be associated with a suppression of the outgoing heat flux due to the presence of magnetic fields. To see whether the heat flux term contribution depends on the presence of the magnetic field structures, we calculated the relative contribution of the terms in the energy equation for electrons: $\frac{\partial E_e}{\partial t} = -\nabla \cdot (E_e v) - P_e \nabla \cdot v - \nabla \cdot q_e + Q_{las}$. Here, $E_e = \frac{3}{2}k_B n_e T_e$ is the internal electron energy density, v is the plasma flow velocity, $P_e = k_B n_e T_e$ is the electron pressure, q_e is the electron heat flux, and Q_{las} is the laser heating. It turns out that the heat flux contribution $|\nabla \cdot q_e|$ is small compared to $|P_e \nabla \cdot v|$ and $|\nabla \cdot (E_e v)|$ around the temperature peak ($10 \leq z/d_i \leq 30$) in the
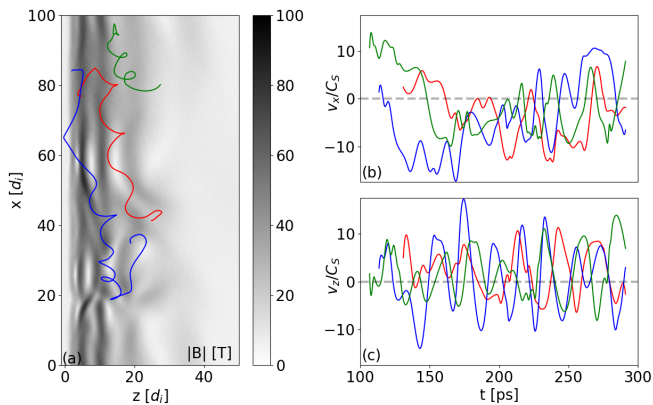
FIG. 5. (a) Selected electron trajectories from the simulation with $I = 10^{14}$ W/cm^2, $L_x = 100d_i$ overplotted with magnetic field amplitude distribution at the end of the simulation ($t = 300$ ps). (b,c) Variations of electron velocities v_x and v_z over time. Electron gyrations are clearly visible in both physical and velocity spaces.

magnetized case, and becomes dominant in the "$B = 0$" simulation for a similar laser heating power (difference in Q_{las} is within 30%). The details of heat conduction in a self-magnetized PIC simulation will be addressed in future work. Another notable difference between the magnetized and unmagnetized simulations is the electron temperature anisotropy (Fig. 4d), where the "$B = 0$" run develops a significantly larger level of anisotropy. This anisotropy is persistent throughout the simulation, as the magnetic fields are prohibited from amplifying via the instabilities. Magnetic fields, much like collisions, will relax the anisotropy over time[27], consistent with Figure 4d.

To illustrate the importance of the magnetic fields in the plasma dynamics, we perform an electron tracking analysis. Figure 5 depicts the influence of magnetic fields on the electron trajectories. Here, we show three selected trajectories, which are representative of the typical behavior of a large fraction of electrons. Figure 5a shows particle trajectories overplotted on the magnetic field magnitude at $t = 300$ ps. Electrons perform gyrations and their motion is restricted along the z axis. Figs. 5b,c demonstrate gyrations in the velocity space. The gyration period of these particles is ~ 25 ps and consistent with the gyration in a few Tesla magnetic fields that are observed in our simulations. Therefore, we conclude that magnetic fields alter plasma behavior by suppressing heat conduction out of the ablation front, contributing to the expanding plasma evolution at later times, as shown in Figs. 4b-d.

To qualitatively explain the emergence of Weibel magnetization in different laser-target interaction regimes, we propose a simple parameter based on the growth rate of a semi-collisional electron Weibel instability. Following Ref.[25], the collisional electron Weibel growth rate is:

$$\gamma_{eW,\text{coll}} = \gamma_{eW0} - \frac{A}{A+1}\nu_{ei}. \qquad (2)$$

Here, γ_{eW0} is the collisionless electron Weibel growth rate calculated for the fastest growing mode, given by Eq. 1. The electron-ion collision rate, ν_{ei}, is calculated as follows[24]:

$$\nu_{ei} = \frac{4}{3}\left(\frac{2\pi}{m_e}\right)^{1/2}\frac{n_e Z e^4 \ln \Lambda}{(k_B T_e)^{3/2}}, \qquad (3)$$

where m_e is the electron mass, n_e and T_e are the electron number density and temperature, Z is the ion charge state, k_B is the Boltzmann constant, and $\ln \Lambda$ is the Coulomb logarithm. The ratio of collisionless to collisional contributions to the growth rate (first and second terms on the RHS of Eq. 2) is given by the following.

$$\Gamma \equiv \frac{(A+1)\gamma_{eW0}}{A\nu_{ei}} \approx 5.6 \cdot 10^{-4}\frac{\sqrt{A}}{Z\ln\Lambda}(T_e[\text{eV}])^2\left(\frac{n_e}{n_{\text{cr},0}}\right)^{-1/2} \qquad (4)$$

Here, $n_{\text{cr0}} \approx 1.1 \cdot 10^{21}$ cm^{-3} is the critical electron density for a 1 micron laser. The coronal electron temperature can be estimated based on the laser and material properties using Ref.[39], which derives plasma properties from steady-state laser ablation (see Ref.[31], Eq. 15). Now, assuming anisotropy is weakly dependent on electron temperature and density and is fixed at $A = 0.01$ (a conservative anisotropy value expected for realistic electron mass and speed of light, as seen in Fig. 6), ignoring the $\ln \Lambda$ dependence on temperature and density and fixing it to 10, and choosing the electron density to be equal to the critical density $n_e = n_{\text{cr}} = n_{\text{cr0}} \cdot (\lambda[1\,\mu\text{m}])^{-2}$, we can obtain a simple parameter that depends solely on laser intensity, wavelength, and material properties:

$$\Gamma \approx 2\frac{\mu^{2/3}}{Z^{5/3}}\left(\frac{\lambda}{1\,\mu\text{m}}\right)^{11/3}\left(\frac{I}{10^{13}\,\text{W/cm}^2}\right)^{4/3}. \qquad (5)$$

Here, μ is the atomic mass and Z is the mean charge state of ablated plasma. If Γ is significantly larger than one, we could expect development of electron Weibel instability. For an Al target with $I = 10^{13}$ W/cm^2, $\Gamma \approx 0.25$, predicting the suppression of Weibel instability, which is consistent with our low-intensity, "unmagnetized" simulations in Fig. 1c and in Ref.[31]. For $I \geq 4 \cdot 10^{13}$ W/cm^2, we enter a regime with $\Gamma \approx 1.5$, where our model predicts Weibel development, and is indeed supported by the parametric scan in Fig. 1c. Auxiliary simulations for a carbon target ($\mu = 12.011$, $Z = 6$) with $\lambda = \{0.532, 1.064\}\,\mu$m laser wavelengths and $I = \{0.8, 2\} \cdot 10^{14}$ W/cm^2 laser intensities were also conducted to test wavelength and material dependence. The Γ parameter correctly predicted electron Weibel behavior in all cases: the growth was suppressed for the $I = 0.8 \cdot 10^{14}$ W/cm^2, $\lambda = 0.532\,\mu$m

case, and Weibel filaments developed for all other parameter cases. We therefore can estimate the emergence of the Weibel instability based on a simple argument formulated with the Γ parameter. Eq. 5 may be used as a simple tool to estimate the importance of the Weibel instability for the experimental parameters of interest.

We should note that Eq. 5 is based on a one-dimensional steady-state ablation theory[39], and does not account for heat flux limitation, radiative energy losses, and utilizes the ideal gas equation of state, among other simplifying assumptions. In our derivation, we also made simple assumptions about how anisotropy and Coulomb logarithm depend on laser parameters. Our limited tentative tests of the expressions for different laser and material parameters showed decent agreement of the Γ criterion with the simulations. However, more testing is needed to verify the wide applicability of the present model. Still, it is important to highlight one feature given by Eq. 5, namely, the strong dependence of Γ on laser wavelength: $\Gamma \propto \lambda^{11/3}$. Switching from the first harmonic of the laser to the second harmonic, with all other parameters fixed, reduces Γ by an order of magnitude. Switching to the third harmonic reduces Γ by almost two orders of magnitude! Such a strong dependence is a combination of heating efficiency of a long wavelength laser (in Ref.[39], $T_e \propto \lambda^{4/3}$) and plasma collisionality being proportional to plasma density, which scales as λ^{-2} at the ablation front.

It is instructive to compare our results to findings of other works on the topic of expanding plasma magnetization. Refs.[25,26] concluded that the parameter controlling the transition from Weibel to Biermann or from Weibel to no Weibel is the Knudsen number, $\lambda_{e,\mathrm{mfp}}/L_T$. We calculate this parameter to be ~ 0.3 in our primary simulations, which was found sufficient to develop Weibel in Ref.[26]. The difference in polarization of the self-generated magnetic fields between our study and Refs.[25,26] may be explained by the different geometry of plasma profiles used in the simulations. Both of these studies used bell-shaped density and temperature distributions as the initial conditions, with both density and temperature peaking at the same location. This situation is relevant to the locations around the laser focal spot, where both density and temperature fall off to background plasma values, leading to the "cold" direction being perpendicular to the local temperature gradients. In our case, however, the self-consistent plasma ablation produces a different profile: while our density profiles are similar to ones in Refs.[25,26], our simulations develop a temperature gradient directed outwards within a very localized location, and have a uniform temperature distribution in the expanding plasmas, see Figs. 1a and 4b. Such distributions are more akin to the laser ablation problem we tackled with PSC and FLASH codes here and discussed for lower intensities in Refs.[30,31]. Moreover, if we consider the location of the largest density gradients in our work and in Refs.[25,26], we see that our densities are much larger there. Therefore, gradient-driven Weibel

is collisionally suppressed in our simulations. To summarize, Refs.[25,26] and the present work considered different plasma profiles, which potentially arise at different locations within laser-heated plasmas, so there is no contradiction per se.

Another important factor explaining the difference in filament geometry is the finite laser spot size. Our current 2D simulations are conducted with a uniform transverse laser intensity profile and with periodic boundary conditions, which can be thought of as mimicking a central slice of a much larger laser spot. This allows magnetic filaments to be up to L_x in size, and Fig. 3 demonstrates that the typical structure size along x is larger than along z. However, by considering finite laser spot sizes, we may amend the permissible Weibel mode values by introducing Biermann fields around the focal spot, effectively reducing the box size for the Weibel instability, as seen in our auxiliary simulations. Therefore, we believe that by considering a finite laser spot size, we may observe results more in line with the findings by Refs.[25,26]. The role of the laser spot size and potential interplay with the Biermann battery magnetic field generation will be discussed in separate work.

Laser heating plays an important role in Weibel magnetogensis. Our auxiliary simulations showed that turning off laser heating 0.1 ns into the simulation (rather than leaving it on) results in a very fast plasma cooldown driven by plasma expansion. Thus, one of the roles of the laser heating is sustaining and, possibly, increasing the temperature of the expanding plasmas. Other works have proposed that the inverse Bremsstrahlung heating can directly produce anisotropic distributions[40], since the electrons oscillate within the transverse laser fields during laser-plasma interaction, and can have preferential heating directions. In our current implementation of the laser heating module[29], the laser heats plasma without adding anisotropy in the electron distribution, thus no direct effect of laser heating on anisotropy is expected. We conducted a series of numerical tests, verifying that the laser heating module does not produce significant anisotropy, see Appendix B for the details. We also initialized our simulation from an analogous FLASH simulation at different output timings, and we observed formation of qualitatively similar magnetic filament structures. Lastly, we conducted a 2D PSC simulation with no laser heating initiated from an analogous FLASH simulation snapshot taken at 0.3 ns. Such plasma was hot enough and expanded fast enough to develop expansion-driven Weibel filaments, although their field amplitudes were suppressed since the plasma was rapidly cooling down. We therefore conclude that the main role of laser heating in our simulations is to sustain high plasma temperature, driving a hot plasma expansion which was the ultimate driver of the Weibel instability.

In conclusion, this paper presents a fully-kinetic simulation of laser-plasma interaction, expansion, and magnetogenesis under long-pulse laser conditions relevant to high-energy-density plasma experiments. We show

that the plasma self-magnetizes above a critical intensity threshold due to expansion-driven Weibel instability producing Hall parameters ($\omega_{ce}\tau_e > 1$) with concomitant modifications to plasma transport. The picture that emerges is that high-temperature ablated plasmas will self-magnetize; accordingly, magnetic field effects should be considered when modeling transport in these plasmas. This investigation was made possible by improving our simulation capabilities associated with collisions[41], laser ray tracing[29], and reinforced by extensive benchmarking[30,31]. More broadly, we showed that fully kinetic simulations are feasible for high-energy-density plasmas, and may be of use for experimental design, interpretation, and cross-code benchmarking.

ACKNOWLEDGEMENTS

[1] J. A. Stamper and B. H. Ripin, Phys. Rev. Lett. **34**, 138 (1975)

[2] P. Nicolaï, M. Vandenboomgaerde, B. Canaud, F. Chaigneau, Phys. Plasmas **7**, 4250 (2000)

[3] R. M. Kulsrud, E. G. Zweibel, Rep. Prog. Phys. **71**, 046901 (2008)

[4] M. Camenzind, Compact Objects in Astrophysics. White Dwarfs, Neutron Stars and Black Holes, Springer 2007

[5] L. M. Widrow, Rev. Mod. Phys. **74**, 775 (2002)

[6] A. Brandenburg, K. Subramanian, Physics Reports, **417**, (1–4), 1 (2005)

[7] L., Biermann, Zeitschrift für Naturforschung **5**, 65 (1950)

[8] E. S. Weibel, Phys. Rev. Lett. **2**, 83 (1959)

[9] P. M. Nilson, L. Willingale, M. C. Kaluza, C. Kamperidis, S. Minardi, M. S. Wei, P. Fernandes, M. Notley, S. Bandyopadhyay, M. Sherlock et al., Phys. Rev. Lett. **97**, 255001 (2006)

[10] J. Zhong, Y. Li, X. Wang, J. Wang, Q. Dong, C. Xiao, S. Wang, X. Liu, L. Zhang, L. An et al., Nat. Phys. **6**, 984 (2010)

[11] Q.-L. Dong, Sh.-J. Wang, Q.-M. Lu, C. Huang, D.-W. Yuan, X. Liu, X.-X. Lin, Y.-T. Li, H.-G. Wei, J.-Y. Zhong et al., Phys. Rev. Lett. **108**, 215001 (2012)

[12] G. Fiksel, W. Fox, A. Bhattacharjee, D. H. Barnak, P.-Y. Chang, K. Germaschewski, S. X. Hu, and P. M. Nilson, Phys. Rev. Lett. **113**, 105003 (2014)

[13] W. A. Farmer, J. M. Koning, D. J. Strozzi, D. E. Hinkel, L. F. Berzak Hopkins, O. S. Jones, M. D. Rosen, Phys. Plasmas **24**, 052703 (2017)

[14] W. Fox, G. Fiksel, A. Bhattacharjee, P.-Y. Chang, K. Germaschewski, S. X. Hu, and P. M. Nilson, Phys. Rev. Lett. 111, 225002 (2013)

[15] C. M. Huntington, F. Fiuza, J. S. Ross, A. B. Zylstra, R. P. Drake, D. H. Froula, G. Gregori, N. L. Kugland, C. C. Kuranz, M. C. Levy et al., Nat. Phys. **11**, 173 (2015)

[16] W. Fox, G. Fiksel, D.B. Schaeffer, D. Haberberger, J. Matteucci, K. Lezhnin, A. Bhattacharjee, M.J. Rosenberg, S.X. Hu, A. Howard, D. Uzdensky, K. Germaschewski, arXiv:2112.03316

[17] M. V. Medvedev and A. Loeb ApJ **526**, 697 (1999)

[18] M. V. Medvedev, L. O. Silva, and M. Kamionkowski, ApJ **642**, L1 (2006)

[19] F. Fiuza, G. F. Swadling, A. Grassi, H. G. Rinderknecht, D. P. Higginson, D. D. Ryutov, C. Bruulsema, R. P. Drake, S. Funk, S. Glenzer, G. Gregori, C. K. Li, B. B. Pollock, B. A. Remington, J. S. Ross, W. Rozmus, Y. Sakawa, A. Spitkovsky, S. Wilks & H.-S. Park, Nat. Phys. **16**, 916 (2020)

[20] C. Zhang, C.-K. Huang, C. Joshi, Reviews of Modern Plasma Physics **7**, 34, (2023)

[21] P. Tzeferacos, A. Rigby, A. F. A. Bott, A. R. Bell, R. Bingham, A. Casner, F. Cattaneo, E. M. Churazov, J. Emig, F. Fiuza et al., Nat. Comm. **9**, 591 (2018)

[22] K. M. Schoeffler, N. F. Loureiro, R. A. Fonseca, and L. O. Silva, Phys. Rev. Lett. **112**, 175001 (2014)

[23] K. M. Schoeffler, N. F. Loureiro, R. A. Fonseca, and L. O. Silva, Phys. Plasm. **23**, 056304 (2016)

[24] A. S. Richardson, NRL Plasma Formulary (2019)

[25] K. M. Schoeffler, L. O. Silva, Phys. Rev. Res. **2**, 033233 (2020)

[26] Z. Zhao, S. He, H. An, Z. Lei, Y. Xie, W. Yuan, J. Jiao, K. Zhou, Y. Zhang, J. Ye et al., Sci. Adv. **10**, eadk5229 (2024)

[27] C. Thaury, P. Mora, A. Héron, J. C. Adam, Phys. Rev. E **82**, 016408 (2010)

[28] C. Thaury, P. Mora, A. Héron, J. C. Adam, T. M. Antonsen, Phys. Rev. E **82**, 026408 (2010)

[29] A. Hyder, W. Fox, K.V. Lezhnin, S. R. Totorica, arXiv:2412.08543

[30] S. Totorica, K. Lezhnin, D. Hemminga, J. Gonzalez, J. Sheil, A. Diallo, A. Hyder, and W. Fox, Appl. Phys. Lett. **124**, 174101 (2024)

[31] K. V. Lezhnin, S. R. Totorica, A. S. Hyder, J. Griff-McMahon, M. B. P. Adams, P. Tzeferacos, A. Diallo, W. Fox, Phys. Plasmas **32**, 022701 (2025)

[32] K. Germaschewski, W. Fox, S. Abbott, N. Ahmadi, K. Maynard, L. Wang, H. Ruhl, A. Bhattacharjee, J. Comp. Phys. **318**, 305 (2016)

[33] B. Fryxell, K. Olson, P. Ricker, F. X. Timmes, M. Zingale, D. Q. Lamb, P. MacNeice, R. Rosner, J. W. Truran, and H. Tufo, ApJS **131**, 273 (2000)

[34] P. Tzeferacos, M. Fatenejad, N. Flocke, C. Graziani, G. Gregori, D.Q. Lamb, D. Lee, J. Meinecke, A. Scopatz, K. Weide, High Ener. Dens. Phys. **17**, 24 (2015)

[35] M.M. Basko, Phys. Plasmas **23**, 083114 (2016)

[36] W. Fox, J. Matteucci, C. Moissard, D. B. Schaeffer, A. Bhattacharjee, K. Germaschewski, S. X. Hu, Phys. Plasmas **25**, 102106 (2018)

[37] G. Kalman, C. Montes, D. Quemada, Phys. Fluids **11**, 1797 (1968)

[38] A. Ramani, G. Laval, Phys. Fluids **21**, 980 (1978)

[39] W. M. Manheimer, D. G. Colombant, J. H. Gardner, Phys. Fluids **25**, 1644 (1982)

[40] K. Bendib, A. Bendib, A. Sid, Laser and Particle Beams, **16**(3), 473 (1998)

[41] S.R. Totorica, W. Fox, K.V. Lezhnin, "Particle collisionality in scaled kinetic plasma simulations", in preparation

[42] D.A. Dickey, W. A. Fuller, J. Amer. Stat. Assoc., 74, 366a, 427 (1979)

Appendix A: Convergence tests

It is important to note that we utilize reduced mass ratio and speed of light parameters to make our simulations feasible, as is commonly done for the PIC simulations of high energy density plasma[22,23,26,36]. One drawback is that the electron mean free path, and thus the anisotropy levels, are overestimated. We performed convergence studies with varied mass ratios ($m_p/m_{e*} = 100, 400, 900, 1836$) and electron rest masses ($m_{e*}c_*^2 = $
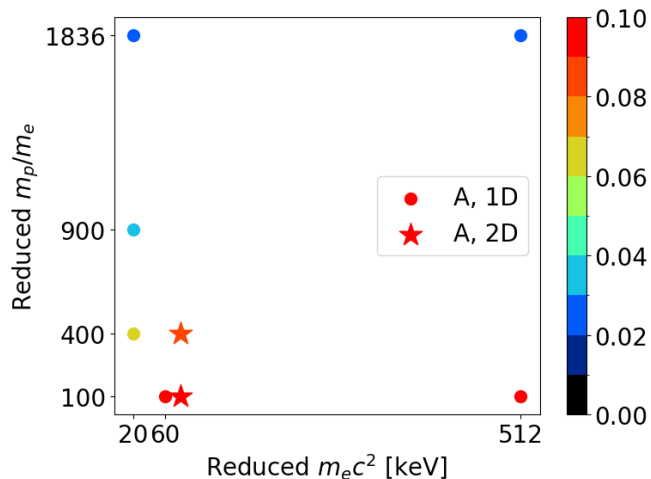
FIG. 6. Electron temperature anisotropy levels for 1D and 2D simulations for various reduced m_p/m_{e*} and c_* parameters. In all considered cases, $A \geq 0.02$.
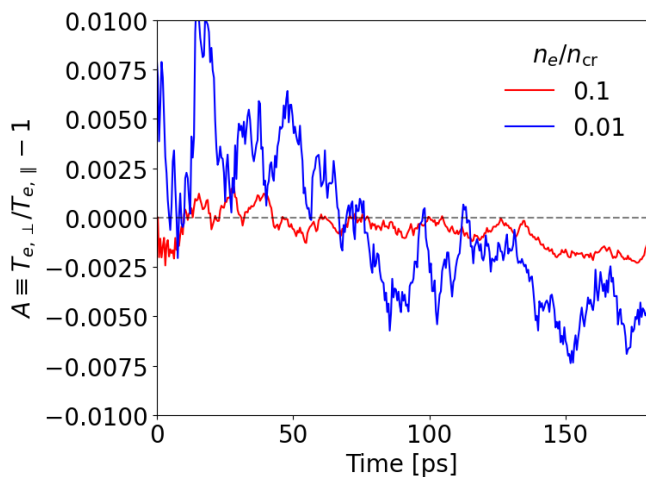

FIG. 7. Anisotropy generated by laser heating for plasma parameters relevant to our 1D/2D PSC simulations for $n_e = 0.1 n_{cr}$ (red) and $n_e = 0.01 n_{cr}$ (blue). The anisotropy generated directly from the laser heating is sign-alternating and negligible compared to the values observed in the primary ablation simulations.

20, 60, 512 keV), which show roughly consistent results for the fastest growing mode. Anisotropy levels decrease as the mass ratio and speed of light approach realistic values, but they do not vanish completely. As shown in Fig. 6, the anisotropy remains at or above $A = 0.02$ even in a full mass ratio and speed of light simulation. Therefore, we conclude that our qualitative results remain valid

despite the use of reduced simulation parameters.

Appendix B: Test of anisotropy development by laser module

Another important check to verify the validity of our simulations is whether the laser heating module generates any plasma anisotropy by itself. While such a process may be physical for a more general inverse Bremsstrahlung heating operator[40], here we consider a heating operator that should not generate any anisotropy by design[29]. To confirm the absence of any sizable level of anisotropy generated by the laser deposition module, we conducted the following tests. We considered a small 1D box of 1 d_i size, resolved by 50 grid cells, with 10^5 electrons per cell at critical density. We fill the simulation box with a uniform Al plasma of either $0.1 n_{cr}$ or $0.01 n_{cr}$ electron densities, with the initial temperature $T_{e0} = 60 \, \text{eV}$ and flow velocity of 500 km/s - typical parameters of the expanding plasma around the region where the magnetic field emerges, see Fig. 1a. Periodic boundary conditions are applied to avoid plasma-boundary interaction effects. A laser with an intensity of 10^{14}W/cm^2 and wavelength of $1.064 \, \mu\text{m}$ is used to heat the initially cold plasma. To isolate the effect of laser heating on plasma anisotropy, we turn off the electromagnetic field solver and collisions, therefore, the particles in the computational domain move ballistically until they are kicked by the laser heating module. It should be noted that using the full field solver and binary collision simulations leads to similar conclusions. The simulation is conducted for 180 ps, a typical timescale of our primary simulations in the paper. Figure 7 depicts the evolution of the mean electron temperature anisotropy inside the simulation box for the initial target densities of $0.1 n_{cr}$ (red line) or $0.01 n_{cr}$ (blue line). First, the maximum anisotropy level is 0.002 for the $0.1 n_{cr}$ case and 0.01 for the $0.01 n_{cr}$ case, as compared to $A \gtrsim 0.1$ in the manuscript. Next, the sign of the anisotropy changes over the course of the simulation, in contrast to the primary simulations in the manuscript. To determine whether the evolution of anisotropy can be characterized as a random walk, we applied the statistical Augmented Dickey–Fuller (ADF) test[42] to the anisotropy time series. The first 10 picoseconds were excluded since rapid laser heating occurs. We conclude that the laser heating module does not generate the anisotropy by itself. The resulting p-values for the presented anisotropy curves are 0.207 and 0.368 for $n_e = 0.1 \, n_{cr}$ and $0.01 \, n_{cr}$, respectively. At the 95% significance level, we therefore fail to reject the null hypothesis, meaning that the anisotropy curves are consistent with the random walk hypothesis.